SUPPLEMENTARY DATA

Precursor Chemistry Governing Morphology and Cation Disorder in $AgBiS_2$ Solar Absorber for Photoelectrochemical Water Splitting

Dayeon Lee, Neul Ha, Jaemin Park, Jisu Jung, Jaewook Lee, Ji Hoon Kim, Sang Uck Lee, Dong-Won Kang, Kaiying Wang and Wooseok Yang*

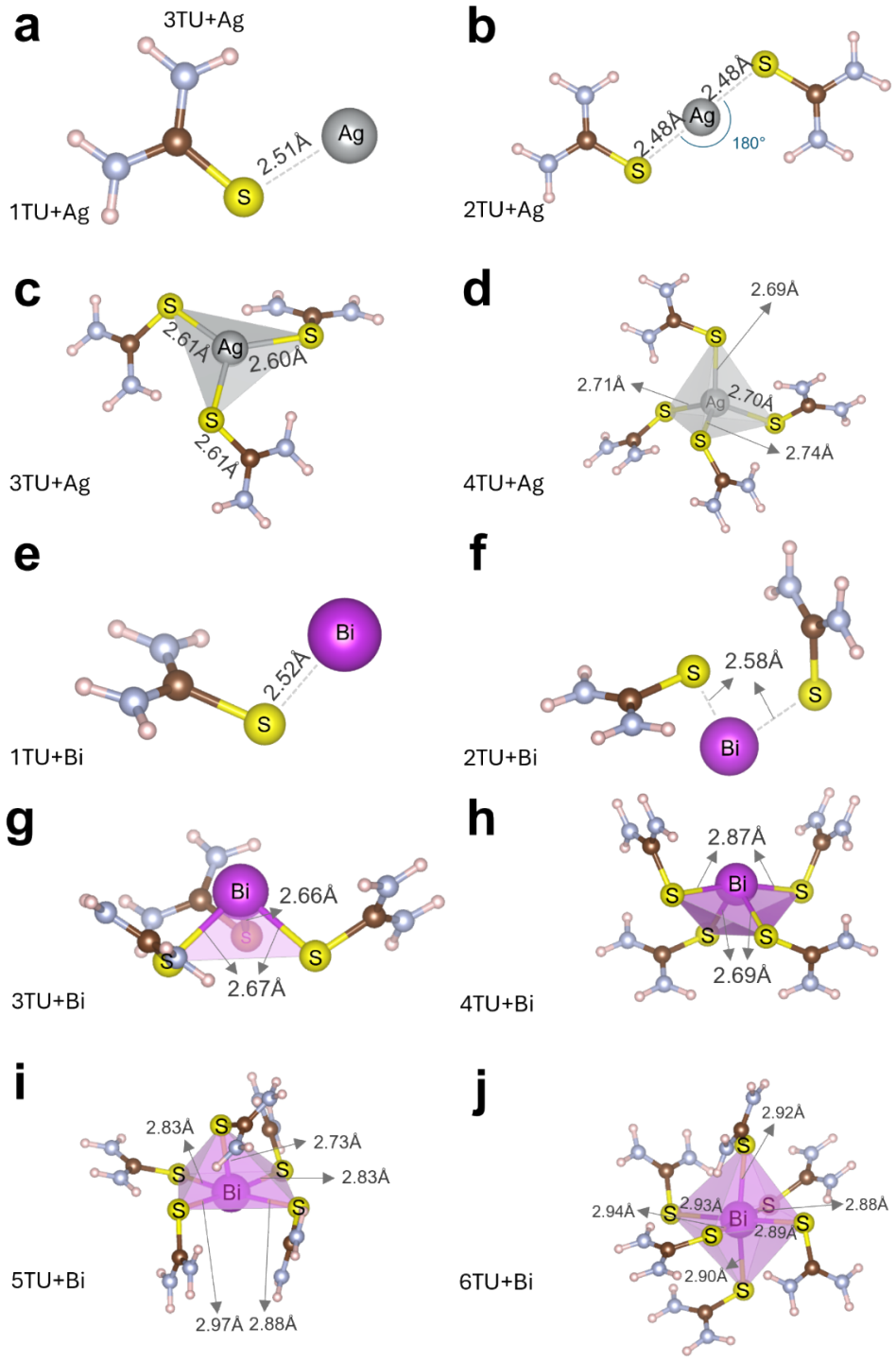

Figure S1. Coordination geometries of metal cations with TU ligands: (a-d) Ag^{+} with TU and (e-j) Bi^{3+} with TU.

Table S1. Quantitative summary of calculated and experimental Raman peak positions for the C=S stretching mode, comparing pure TU and TU coordinated with Ag and Bi. This table provides the specific wavenumbers corresponding to the coordination-induced shifts illustrated in Figure 1d-e.

	TU	TU+Ag	TU+Bi
Calculation (cm^{-1})	744	727	731
Experimental (cm^{-1})	746	744	742

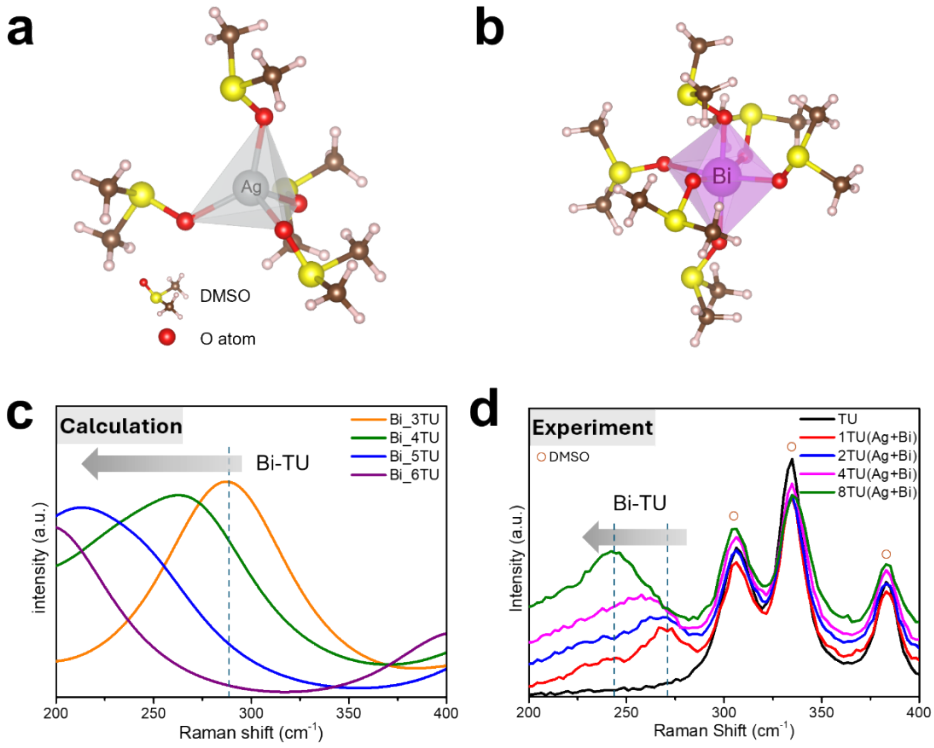

Figure S2. (a-b) Optimized coordination geometries of (a) Ag^{+} and (b) Bi^{3+} ions with DMSO ligands, as obtained from calculations. (c) Simulated Raman spectra of Bi–TU complexes with varying coordination numbers (n = 3–6). The Bi–TU peak shifts to lower wavenumbers with increasing TU coordination. (d) Experimental Raman spectra of TU solutions containing both Ag^{+} and Bi^{3+} at various TU/M ratios (n = 1, 2, 4, 8). The gray arrows and dashed lines indicate the characteristic Bi–TU peak position and its blue-shift trend with increasing TU coordination.

Table S2. Quantitative summary of Raman peak positions for the C=S stretching mode as a function of nTU(M) ratios (n = 1, 2, 4, 8). This table provides the specific wavenumbers corresponding to the coordination-induced shifts in nTU(Ag) and nTU(Bi) conditions illustrated in Figures 2a-d.

	TU	TU+Ag	TU+Bi
1 (cm^{-1})	744	727	731
2 (cm^{-1})	746	744	742
4 (cm^{-1})	746	744	742
8 (cm^{-1})	746	742	742

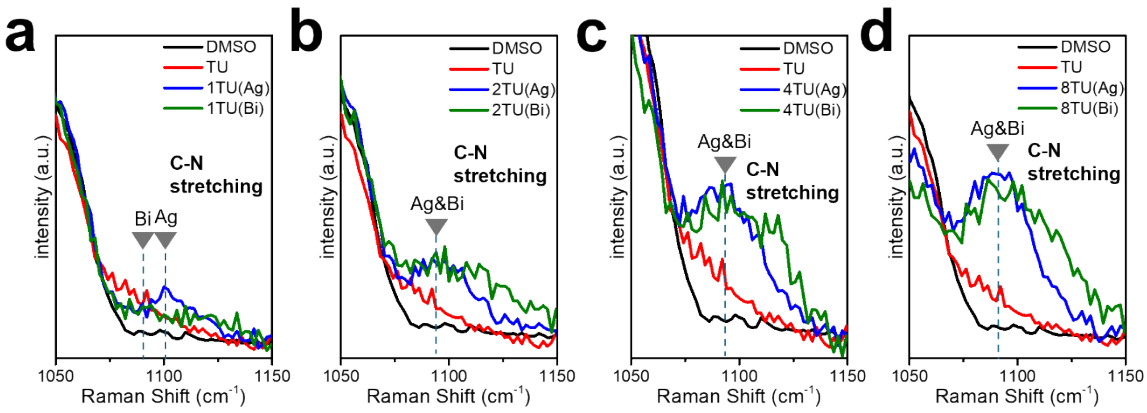

Figure S3. (a–d) Raman spectra of solutions containing either Ag^{+} or Bi^{3+} ions at varying TU/M ratios (n = 1, 2, 4, 8). The dashed lines and gray arrows indicate the C–N stretching peak positions corresponding to nTU(Ag) and nTU(Bi) complexation, highlighting spectral shifts upon metal coordination.

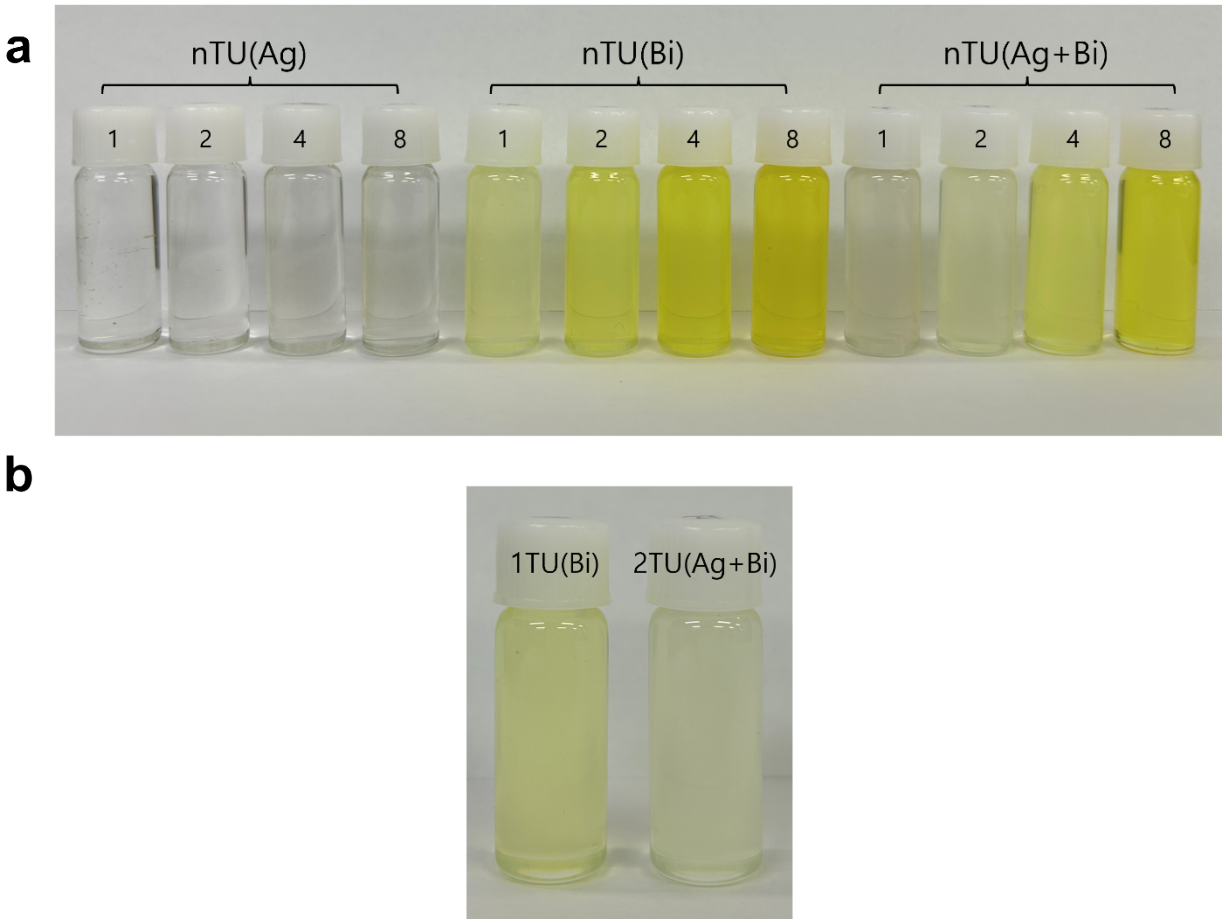

Figure S4. Photographs of solutions under various metal ion conditions at different TU/M ratios (n = 1, 2, 4, 8). (a) Solutions with increasing TU/M ratios (n=1, 2, 4, 8): nTU(Ag) solutions (left four vials), nTU(Bi) solutions (middle four vials), and nTU(Ag+Bi) solutions (right four vials). In all preparations, the concentration of each metal precursor (Ag or Bi) is maintained at 0.2 M. (b) Comparison of 1TU(Bi) solution (left) and 2TU(Ag+Bi) solution (right). The 1TU(Bi) solution exhibits a more intense yellow color than 2TU(Ag+Bi) solution.

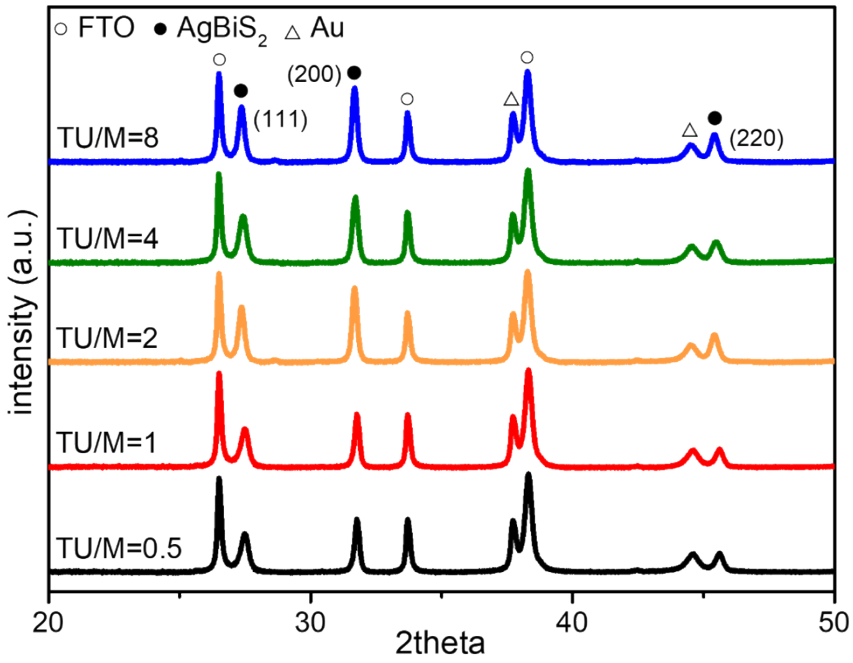

Figure S5. (a) XRD patterns of $AgBiS_2$ thin films. The films were deposited on Au/FTO substrates using precursor solutions with varying TU/M ratios, followed by annealing at 200 °C. All samples were fabricated at 3000 rpm with 6 coating cycles.

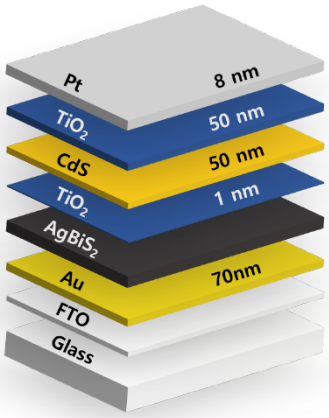

Fabricated Photocathode

Figure S6. Schematic structure and layer thicknesses of the FTO/Au/$AgBiS_2$/TiO_2/CdS/TiO_2/Pt photocathode. The labeled values indicate the thickness of each layer.

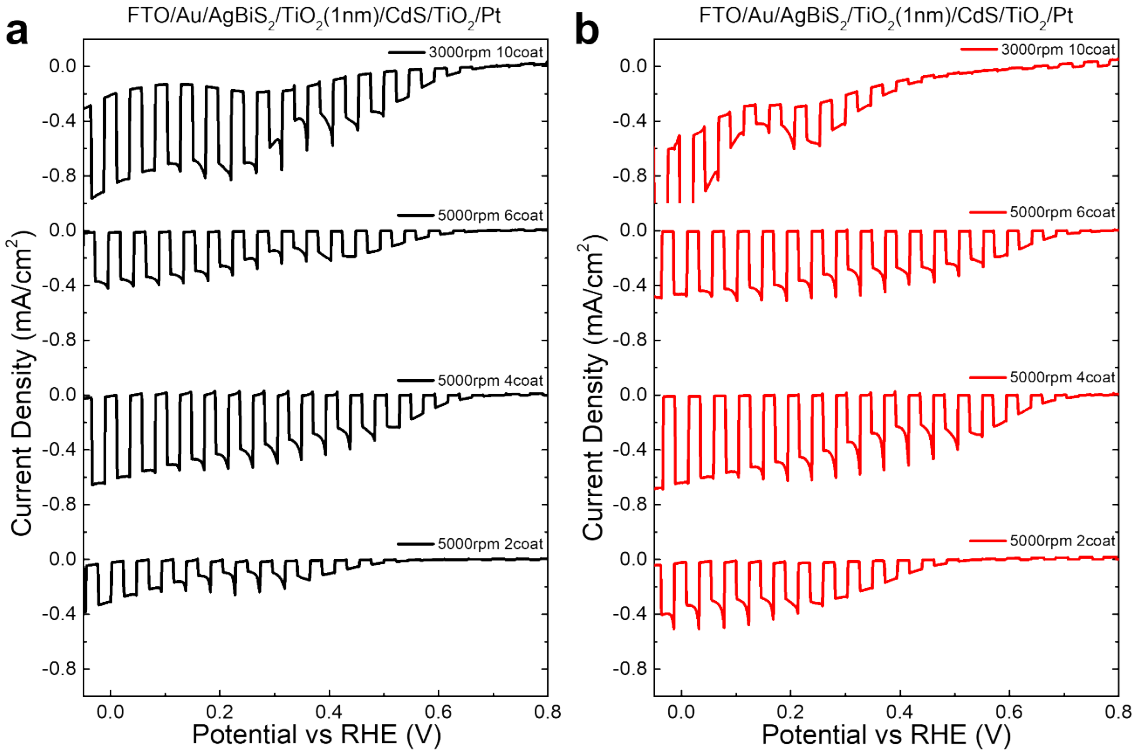

Figure S7. Chopped-light LSV curves of FTO/Au/$AgBiS_2$/TiO_2(1 nm)/CdS/TiO_2/Pt photocathodes with different $AgBiS_2$ deposition conditions at TU/M ratios of (a) 1 and (b) 8. For all devices in this optimization set, the TiO_2 electron transfer layer was deposited for 1000 cycles and no N_2 purging was performed during the measurements. All other fabrication and experimental parameters remained identical to those described in the main text and Experimental Section.

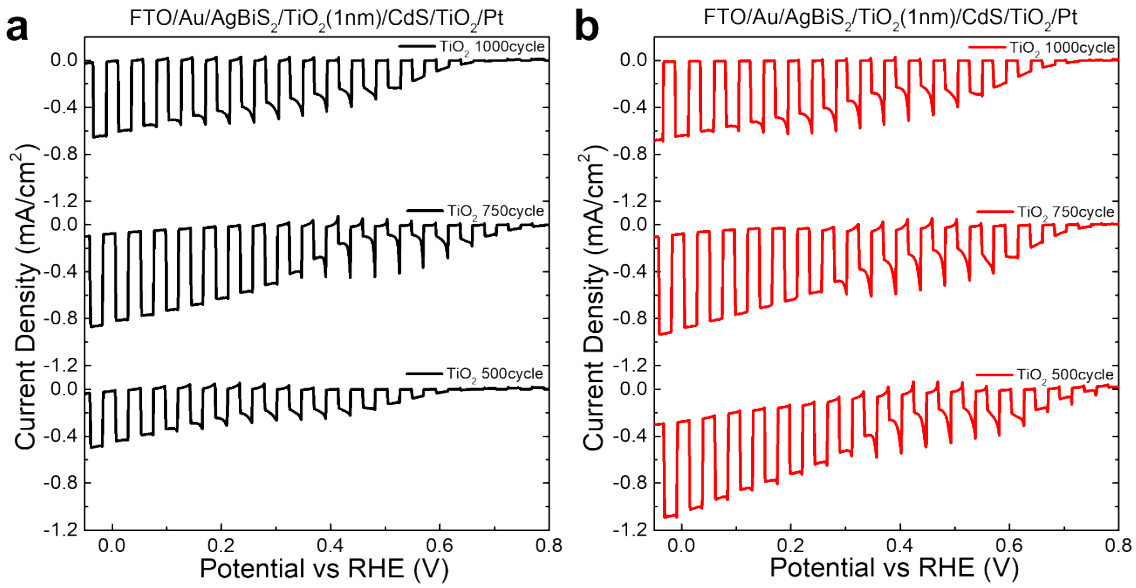

Figure S8. Chopped-light LSV curves of FTO/Au/$AgBiS_2$/TiO_2(1 nm)/CdS/TiO_2/Pt photocathodes with different TiO_2 electron transfer layer deposition conditions at TU/M ratios of (a) 1 and (b) 8. The TiO_2 layers were deposited for 1000, 750, and 500 cycles, respectively. No N_2 purging was performed during the measurements. All other fabrication and experimental parameters remained identical to those described in the main text and Experimental Section.

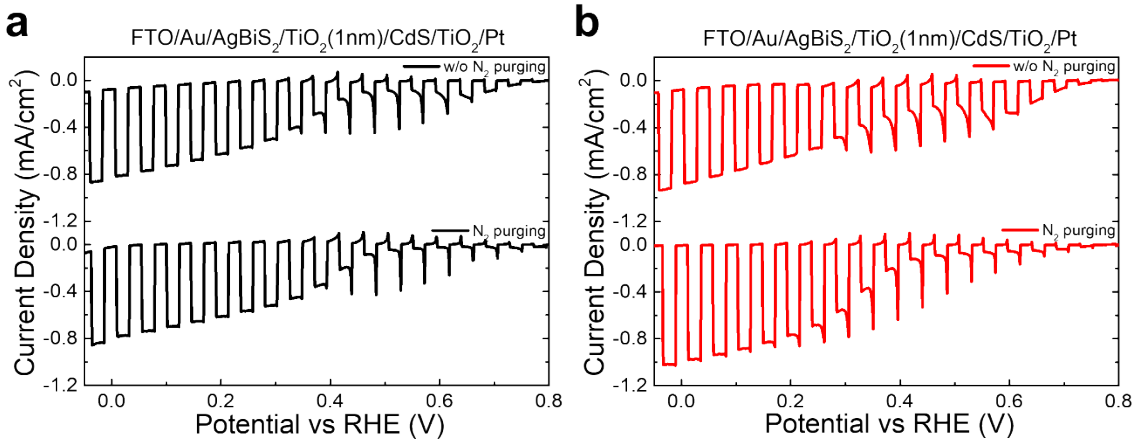

Figure S9. Chopped-light LSV curves of FTO/Au/$AgBiS_2$/TiO_2(1 nm)/CdS/TiO_2/Pt photocathodes measured without (top) and with (bottom) N_2 purging at TU/M ratios of (a) 1 and (b) 8. All other fabrication and experimental parameters remained identical to those described in the main text and Experimental Section.

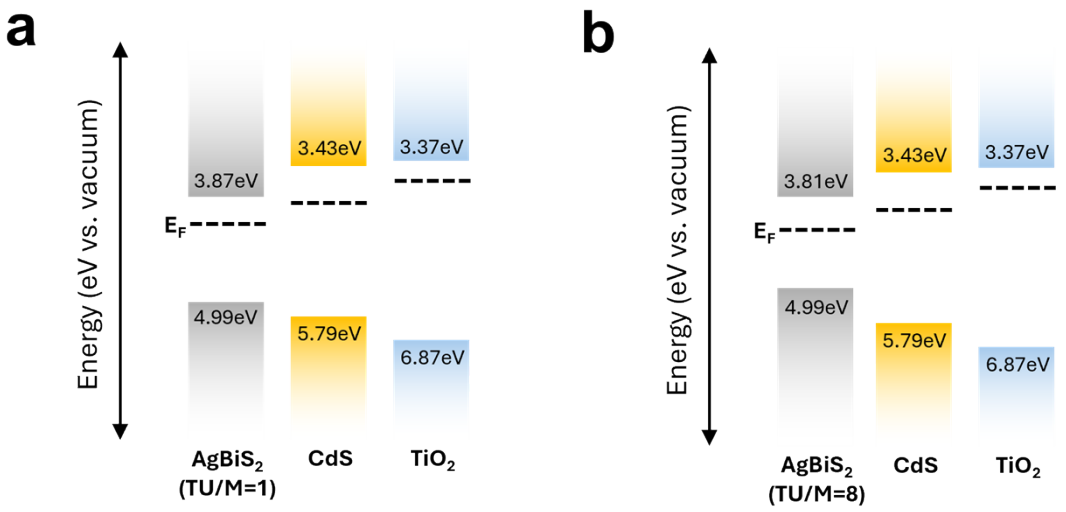

Figure S10. Energy band diagrams of the $AgBiS_2/CdS/TiO_2$ photocathode constructed from ultraviolet photoelectron spectroscopy (UPS) and UV–vis measurements. (a) TU/M = 1 and (b) TU/M = 8 conditions. The diagrams illustrate the shifts in energy levels of $AgBiS_2$ as a function of TU coordination, while the energy levels of CdS and TiO_2 remain constant. Note that Fermi level alignment between the layers is not achieved under these conditions, reflecting distinct interfacial energetics at different TU/M ratios.

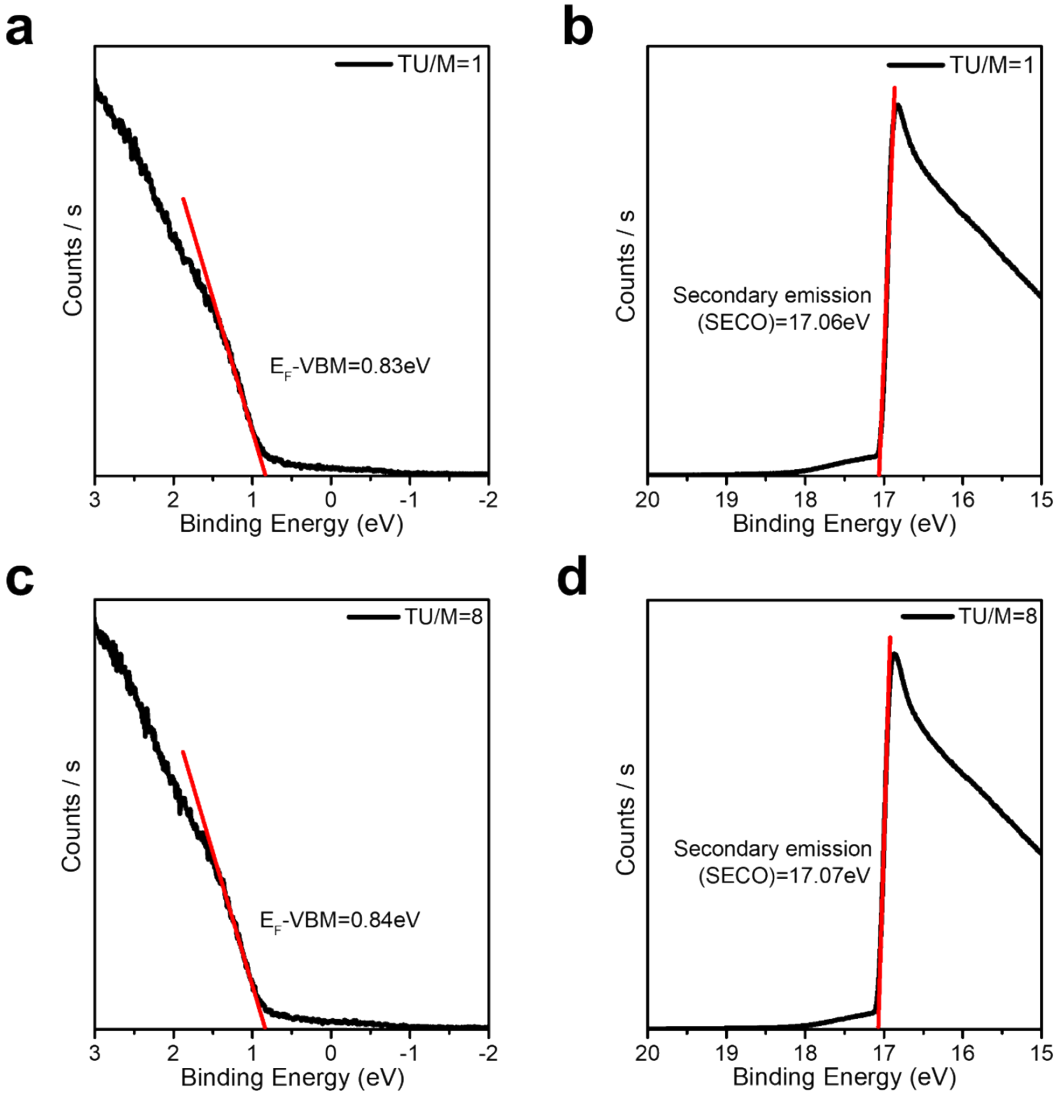

Figure S11. Ultraviolet photoelectron spectroscopy (UPS) spectra of $AgBiS_2$ thin films synthesized at TU/M molar ratios of 1 and 8. (a, b) UPS spectra for TU/M = 1: (a) valence band onset, used to determine the energy difference between the Fermi level and valence band maximum (E_F − VBM = 0.83 eV); (b) secondary electron cutoff (SECO = 17.06 eV). (c, d) UPS spectra for TU/M = 8: (c) valence band onset (E_F − VBM = 0.84 eV); (d) SECO = 17.07 eV. These results were used to construct the energy band diagrams in **Figure 5**d-f and **Figure S10**.

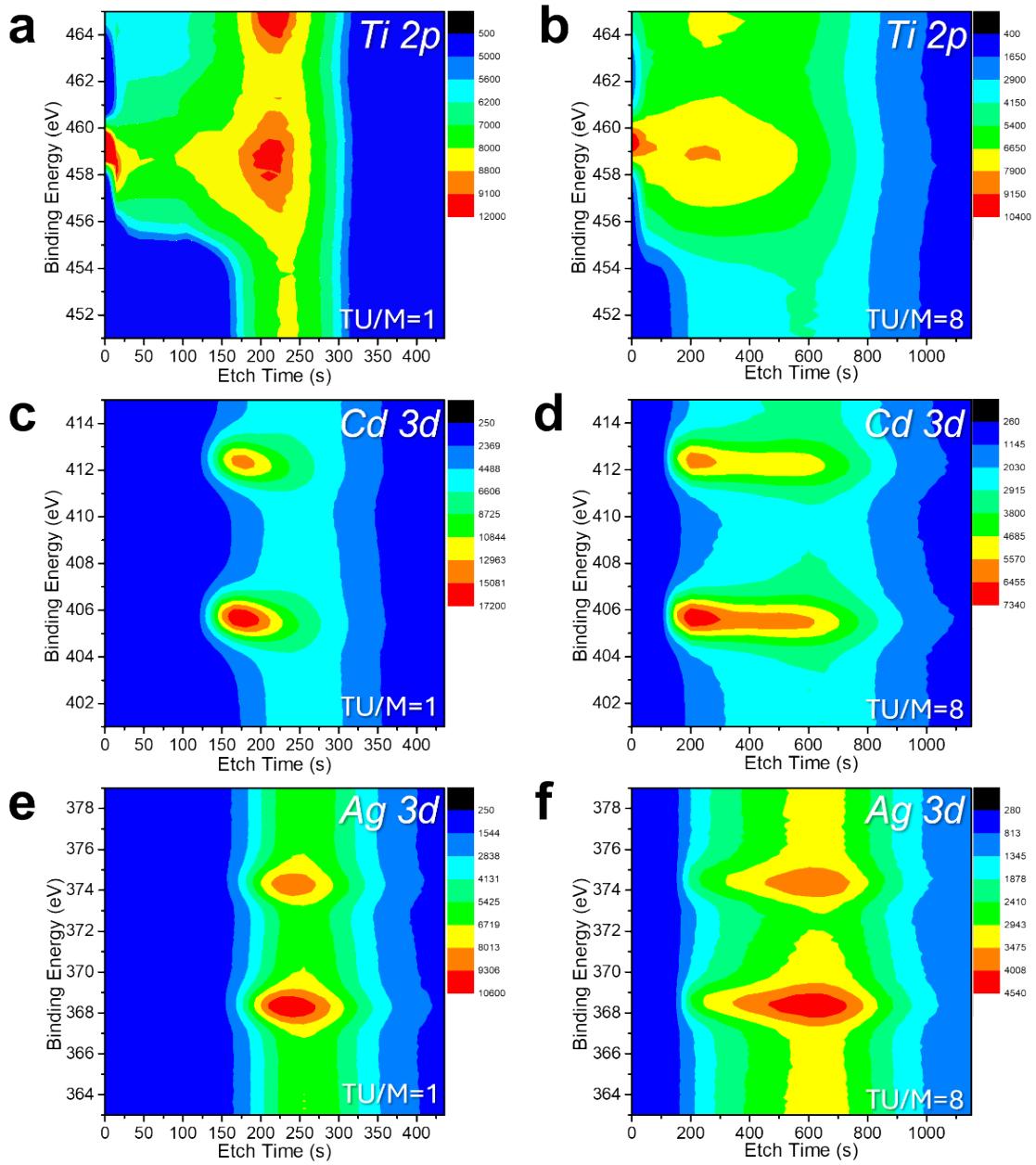

Figure S12. Elemental depth profile contour plots of Ti 2p (a, b), Cd 3d (c, d), and Ag 3d (e, f) XPS signals for $AgBiS_2$/CdS/TiO_2 photocathodes prepared with TU/M ratios of 1 (left column) and 8 (right column). The intensity variations along the etch time axis reflect the distribution and relative abundance of each element within the photoelectrode. Longer etch times correspond to deeper layers.